

X-ray and strong lensing mass estimate of MS2137.3–2353

A. Donnarumma^{1,2,3*}, S. Ettori^{2,3}, M. Meneghetti^{2,3}, L. Moscardini^{1,3}

¹ Dipartimento di Astronomia, Università di Bologna, via Ranzani 1, I-40127 Bologna, Italy

² INAF-Osservatorio Astronomico di Bologna, via Ranzani 1, I-40127 Bologna, Italy

³ INFN, Sezione di Bologna, viale Berti Pichat 6/2, I-40127 Bologna, Italy

Accepted ????. Received ????

ABSTRACT

We present new mass estimates of the cluster of galaxies MS2137.3–2353, inferred from X-ray and strong lensing analyses. This cluster exhibits an outstanding strong lensing configuration and indicates a well-relaxed dynamical state, being most suitable for a mass reconstruction which combines both techniques. Despite this, several previous studies have claimed a significant discrepancy between the X-ray and the strong lensing mass estimates. The primary aim of this paper is to address and explain this mismatch.

For this purpose, we have analysed *Chandra* observations to recover the profiles of the intra-cluster medium properties and, assuming a functional form for the matter density, the total mass distribution. The notable strong-lensing features of MS2137.3 allow us to reconstruct its projected mass in the central regions with good accuracy, by taking advantage of the lensing inversion code *Lenstool*. We compare the results obtained for both methods. Our mass estimates for MS2137.3 are in agreement within errors, leading to a mean, extrapolated value of $M_{200} \simeq 4.4 \pm 0.3 \times 10^{14} M_{\odot}$, under the assumption of the Navarro-Frenk-White (NFW) mass profile. However, the strong lensing mass estimate is affected by the details of the BCG mass modeling, since the radial arc is a very sensitive probe of the total mass derivative in the central region. In particular, we do not find evidence for a high concentration for the NFW density profile, as reported in some earlier works.

Key words: galaxies: clusters: individual, MS2137.3-2353 – cosmology: dark matter, gravitational lensing – X-ray: galaxies: clusters.

1 INTRODUCTION

According to the hierarchical growth of cosmic structures implied by the concordance model, clusters of galaxies are the most recent gravitationally-relaxed structures. They are ideal cosmological tools (see e.g. Voit 2005; Borgani 2006; Tozzi 2007; Diaferio, Schindler & Dolag 2008), provided we have a reliable measurement of their masses. The most promising techniques for estimating cluster masses are via X-ray and gravitational lensing analyses.

Cluster X-ray luminosity is mainly due to diffuse plasma emission: the deep potential wells produced by the dark matter component heat the intra-cluster medium (ICM) to temperatures of some keV, at which point X-ray photons are emitted through thermal bremsstrahlung. The X-ray emissivity is proportional to the square of the gas density, thus it is an excellent tracer of the three-dimensional cluster potential. However, X-ray measurements of cluster masses imply the assumption of hydrostatic equilibrium of the ICM with the dark matter potential and of spherical symmetry of the cluster mass distribution. Hence the total mass profile can be

inferred from the radial profiles of temperature and gas density.

On the contrary, the gravitational lensing effect, i.e. the light deflection due to the space-time curvature induced by massive objects, allows for the determination of the projected surface mass density of the lens, regardless of its dynamical state or the nature of the intervening matter. However, this effect is determined by all massive structures along the line of sight, so lensing mass measurements are subject to foreground and background contaminations. Moreover, the lensing effect is very sensitive to features of the mass distribution such as its ellipticity and asymmetry, as well as to the presence of substructures (Meneghetti et al. 2007), which complicate the mass reconstruction.

The X-ray and lensing methods are clearly complementary, allowing in principle to combine 2- and 3-dimensional constraints to obtain a reliable mass estimate (see for example Allen 1998; Ettori & Lombardi 2003; Bradač et al. 2008); a limit to such a comparative analysis is the significant disagreement between strong lensing and X-ray mass estimates claimed in the literature (Wu & Fang 1996; Smail et al. 1997; Ota et al. 2004; Voigt & Fabian 2006; Gitti et al. 2007; Halkola et al. 2008). Many convincing explanations have been suggested, but to date, the discrepancy between X-ray and strong lensing results appears to be an

* E-mail: annamaria.donnarumma2@unibo.it

issue.

Moreover, galaxy clusters enable one to determine dark matter (DM) halo density profiles, being mainly composed by dark matter. As a consequence, they could help in verifying the Λ CDM model predictions for the formation of cosmic structures: for example, if DM density profiles can be approximated on all mass scales by “universal” profiles, such as the Navarro-Frenk-White (NFW) profile (Navarro, Frenk & White 1995, 1997), as predicted by N-body simulations of structure formation in hierarchical collapse models. In particular, the inner DM density slope is a very debated issue: several studies have argued that it could deviate from the NFW predictions (Moore et al. 1998; Jing & Suto 2000; Gao et al. 2008). Galaxy clusters play a crucial role in solving this issue, since they allow to distinguish between cuspy and flat profiles due to their low concentrations. An emblematic case in both of these debates is MS2137.3-2353: even though this cluster has a relaxed appearance, there is still disagreement both regarding its inner slope value (Dalal & Keeton 2003; Sand et al. 2004; Gavazzi 2005a; Sand et al. 2008) and the X-ray and strong lensing mass estimates (Gavazzi et al. 2003; Gavazzi 2005b; Comerford et al. 2006; Comerford & Natarajan 2007).

In this work we will focus on the latter topic. We present new X-ray and strong lensing mass estimates, based respectively on a non-parametric analysis of gas density and temperature profiles through *Chandra* observations, and on a strong lensing reconstruction, performed using the *Lenstool* analysis software (Kneib et al. 1996; Jullo et al. 2007).

This paper is organised as follows. In § 2 we will discuss our X-ray analysis, focusing on data reduction and on the method applied to recover the total and gas mass profiles, and we will summarize our X-ray results. The strong lensing analysis is presented in § 3, where we will briefly discuss our main findings. We will compare the X-ray and strong lensing results in § 4: a comparison with previous analyses can be found in § 5. Finally, we will summarize our results and draw our conclusions in § 6.

Throughout this work we assume a flat Λ CDM cosmology, with matter density parameter $\Omega_m=0.3$, cosmological constant density parameter $\Omega_\Lambda=0.7$, and Hubble constant $H_0 = 70 \text{ h}^{-1} \text{ km s}^{-1} \text{ Mpc}^{-1}$. Unless otherwise stated, all uncertainties are referred to a 68% confidence level.

2 X-RAY ANALYSIS

2.1 X-ray data reduction

MS2137.3-2353 is a rich, X-ray luminous cluster at $z = 0.313$ (Stocke et al. 1991): within a radius of $\simeq 0.7$ Mpc, its luminosity in the [0.5–8.0] keV band¹ is $\simeq 1.4 \times 10^{45} \text{ erg s}^{-1}$. This cluster exhibits several indications of a well relaxed dynamical state, for instance the absence of evident substructures and a central X-ray surface brightness peak, associated with a cool core. These characteristics support the hypothesis of hydrostatic equilibrium underlying our X-ray mass estimate.

We performed our X-ray analysis on two datasets retrieved from the *Chandra* archive (see Table 1 for observation log); both the observations were telemetered in Very Faint mode, and were reduced accordingly. Another *Chandra* dataset is currently available (ID 4974, start date: 2003-11-13, total exposure time: 58.0 ks,

¹ The X-ray luminosity was derived fitting the cluster integrated spectra in the radial range [0 – 0.7] Mpc using the *XSPEC* analysis package.

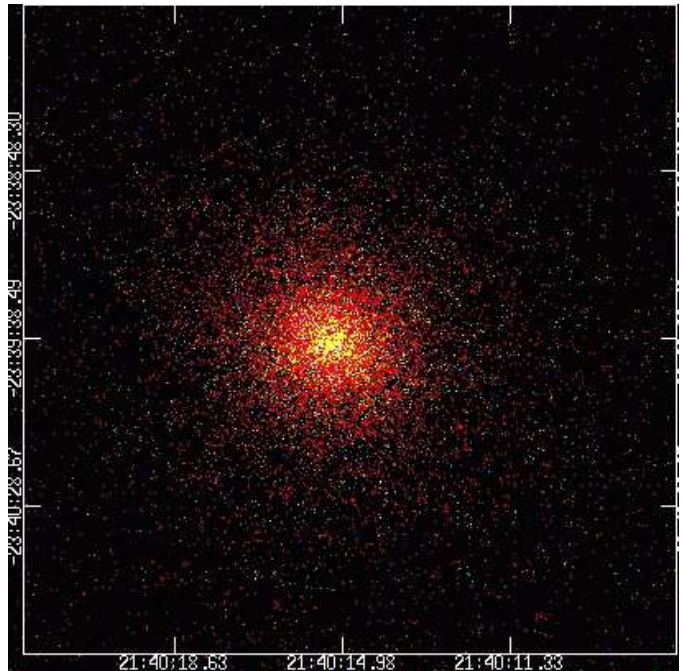


Figure 1. True colour image of MS2137; red, green and blue colours correspond to [0.5–2.0], [2.0–4.0], [4.0–8.0] keV bands, respectively. The size of the field of view is $200'' \times 200''$.

Table 1. *Chandra* observations summary.

Obs.ID	Start Time	Total Expos. [ks]	Net Expos.[ks]	PI name
928	1999-11-18 08:37:37	44.17	20.7	Wise
5250	2003-11-18 20:06:43	41.09	25.0	Allen

PI: Allen). The background light curve of this observation presents pronounced flares and a variable quiescent rate. A careful background light curve screening could solve the flaring issue, allowing to disentangle the ICM emission from the spurious signal. However, unlike the observations we used for our analysis, Obs.4974 presents a widely-scattered and variable quiescent count rate. This feature makes it hard to distinguish the cluster emission from possible spurious events, and could affect the background estimate. Moreover, the final net exposure time for this dataset was only $\simeq 16$ ks. So, to prevent systematic errors associated with an incorrect background estimate, we decided to discard this dataset.

The data were reduced using the *CIAO* data analysis package (version 3.4) and the calibration database CALDB 3.4.2; here we summarize briefly the reduction procedure².

We reprocessed the level-1 event files to include the appropriate gain maps and calibration products and to reduce the ACIS quiescent background³. We used the `acis_process_events` tool to check for the presence of cosmic-ray background events, correct for spatial gain variations due to charge transfer inefficiency and re-compute the event grades. We selected the events flagged with

² See the *CIAO* analysis guides for the data reduction: cxc.harvard.edu/ciao/guides/.

³ For a complete discussion on this topic, see cxc.harvard.edu/cal/Acis/Cal_prods/vfbkgnd/index.html.

grades 0, 2, 3, 4 and filtered for the Good Time Intervals associated with the observations. We identified bright point sources using the script `vtpdetect`; the results were subsequently checked through visual inspection. We masked out the point sources and corrected for the discarded area.

A careful screening of the background light curve is necessary to identify background flares (Markevitch et al. 2003). The background light curve was extracted with a time bin size of $\simeq 1$ ks in the energy range [2.5–7] keV, which is the most sensitive to common flares for the S3 BI chip, where the cluster was centered in both observations. We applied the script `analyze_ltcrv` to include only the time periods inside the 3σ range. We compared the S3 background light curve with the one extracted in the S1 chips using the energy range [2.5–6] keV, to check for undetected faint flares, that were not identified. The S3 background light curve was examined using the *ChIPS* facilities to identify and exclude further flaring events; finally we selected only time bins within a factor 1.2 of the apparent quiescent rate, through the script `lc_clean`. At the end of the light curve screening, almost half of the initial exposure time was discarded (see Tab. 1).

2.2 X-ray analysis

Cluster mass measurements derived under the hydrostatic equilibrium hypothesis are strongly dependent on the temperature profile, as demonstrated by Rasia et al. (2006); therefore, any temperature bias could affect the mass estimates. We extracted the background spectrum from the blank-field background data sets provided by the ACIS calibration team, to derive ARF and RESPONSE matrices consistent both with the source and the background spectrum. The blank-sky observations underwent a reduction procedure comparable to the one applied to the cluster data, after being re-projected onto the sky according to the observation aspect information. We derived the background re-normalization factor in the [9.5–11.5] keV band for the Observation 5250 and in the [8.0–9.8] keV band for the Observation 928. The normalization factor was derived in different bands for the two observations because of a difference in the energy upper limit of the FEF (FITS Embedded Function) calibration files associated to the observations (for the latter observation, the upper limit is $\simeq 9.8$ keV). Currently, the energy range defined for the spectrum extraction must match the one in the FEF files to derive a RESPONSE matrix using the *CIAO* package tools⁴. However, the observed flux in both these bands can be safely attributed to the background component, so the difference in the blank-sky renormalization bands has a negligible impact in the subsequent analysis.

The background in the soft band is variable both in time and in space, so we verified whether the soft X-ray background derived by the blank-sky datasets is consistent with the observed one. If they were significantly different, one should take into account this factor in the X-ray spectral fitting. For both datasets we extracted a spectrum in a region free of cluster emission, to which we subtracted a spectrum derived in the same region of the blank-field dataset. We fitted the residuals in the [0.4–1] keV energy band with a MEKAL model, without an absorption component and broadening the normalization fitting range to negative values. The results indicate that a corrective component is not necessary.

2.3 Spectral fitting

We derived the cluster X-ray flux image through the combined, point-source removed images in the energy range [0.3–8.0] keV, properly dividing by the exposure maps for the two observations. The spectra were extracted on concentric, circular annuli centred on the X-ray surface brightness centroid, sized to contain at least 5000 net source counts, up to a net count rate of $\simeq 40\%$. We selected 7 annuli, up to 2.45 arcmin. The X-ray emission appears well centred on the brightest cluster galaxy (BCG). The shift between the estimated X-ray centroid and the BCG center is $\simeq 1$ arcsec: the uncertainty on the X-ray centroid estimate is comparable to the applied smoothing scale (1.5 arcsec). We used the *CIAO* `specextract` tool both to extract the source and background spectra and to construct ancillary-response and response matrices. The spectra were fitted in the [0.6–7.0] keV range, except for the last annulus, where, due to the higher background level, we restricted the analysis to the range [0.6–5.0] keV. We used the *XSPEC* software package (Arnaud 1996) to analyse the spectra, that were fitted adopting an optically-thin plasma emission model (the MEKAL model; Mewe et al. 1985; Kaastra & Mewe 1993), with an absorption component, described by the Tübingen–Boulder model (`tbabs` model; Wilms et al. 2000), to take into account the effect of Galactic absorption on the observed flux.

The Galactic absorption was fixed to the value inferred from radio HI maps in Dickey & Lockman (1990), i.e. $3.55 \times 10^{20} \text{ cm}^{-2}$, with the cluster-averaged values of Galactic absorption derived from the X-ray spectra fit being consistent with the radio value ($3.9 \pm 0.8 \times 10^{20} \text{ cm}^{-2}$ and $4.2 \pm 0.9 \times 10^{20} \text{ cm}^{-2}$ for the Observations 928 and 5250, respectively). Thus the free parameters in our model were the temperature, the metallicity and the normalization of the thermal spectrum.

The spectral data were not rebinned to keep a high spectral resolution: we only grouped the channels to have at least one count in each channel. As a consequence, we applied the *c-stat* statistic to the spectral fitting.

The two observations were at first analysed individually, to assess the consistency of the datasets and to exclude any systematic effects that could influence the combined analysis. A significant difference was detected in the spectral fit results for the most distant radial bin, supposedly for the higher background in Obs.5250. Thus the spectrum relative to Obs.5250 was discarded. We proceeded with the joint analysis of the two datasets, tying the temperature and metallicity parameters and leaving the normalization unlinked. The fit results from the spectral analysis of the two combined datasets are listed in Tab. 2. The resulting metal abundance profile presents a central peak with a smooth external decline, as is generally observed for dynamically relaxed clusters. Moreover, the temperature decrease in the central region associated with the cluster cool core is evident in Fig. 2. Several earlier studies stated that the presence of a cool core, if neglected, could be a possible source of error in the X-ray mass estimate, resulting in an underestimate of the cluster virial temperature and mass (Allen 1998; Hallman et al. 2006; Rasia et al. 2006). On the contrary, if the gas temperature decrement is properly taken into account, cool core clusters should be ideal targets for mass analyses, being typically dynamically relaxed systems. Since our X-ray mass estimate relies directly on the *measured* gas temperature profile, the temperature decrement in the center is not an issue in the mass derivation.

⁴ See cxc.harvard.edu/ciao/bugs/mkwarf.html.

Table 2. X-ray spectral fit results. The analysis was performed in the [0.6–7.0] keV energy range except for the last annulus, where we considered the range [0.6–5.0] keV. The columns list the outer radius of the annulus where the spectral extraction was performed, the best-fit values obtained for the free parameters of the model (i.e. the intra-cluster gas temperature, the normalization of the X-ray spectrum and the metallicity) and the χ -statistic result (the degrees of freedom for each annulus are in square brackets).

SPECTRAL FIT RESULTS				
R_{out} [arcmin]	T_{gas} [keV]	Normalization $\times 10^4$	Metal abundance [Z_{\odot}]	Goodness of fit
0.065	$4.33^{+0.20}_{-0.19}$	$7.03^{+0.25}_{-0.27}$	$0.60^{+0.13}_{-0.11}$	459.2[567]
0.114	$4.22^{+0.19}_{-0.18}$	$7.62^{+0.28}_{-0.29}$	$0.58^{+0.13}_{-0.11}$	514.8[552]
0.17	$4.66^{+0.23}_{-0.21}$	$7.43^{+0.25}_{-0.26}$	$0.52^{+0.12}_{-0.11}$	578.7[579]
0.26	$5.35^{+0.28}_{-0.26}$	$8.67^{+0.25}_{-0.27}$	$0.50^{+0.12}_{-0.10}$	597.0[615]
0.45	$5.88^{+0.29}_{-0.28}$	$11.17^{+0.28}_{-0.30}$	$0.41^{+0.10}_{-0.09}$	670.3[679]
1.0	$5.03^{+0.25}_{-0.23}$	$12.15^{+0.32}_{-0.33}$	$0.38^{+0.10}_{-0.09}$	658.3[740]
2.45 ^a	$3.63^{+0.59}_{-0.43}$	$6.50^{+0.54}_{-0.56}$	$0.40^{+0.30}_{-0.21}$	348.0[291]

^a The results obtained for the last annulus refer to a fit performed for Obs. 928 only.

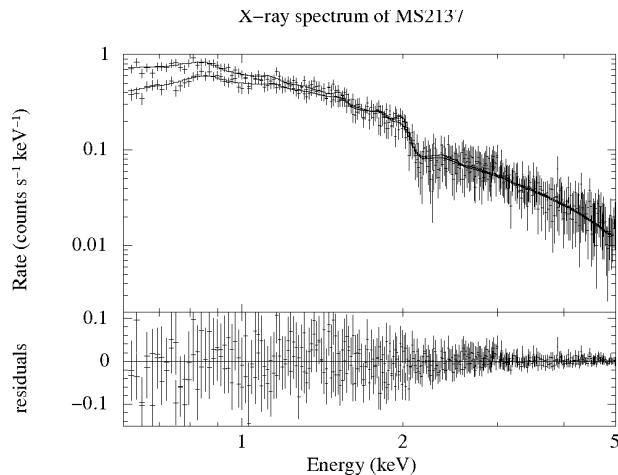


Figure 2. (Top panel) The X-ray spectrum of MS2137, obtained combining Obs. 928 and Obs. 5250. The spectrum was reduced from an aperture of 2.45 arcmin, and shows the energy range [0.6 – 5.0] keV. We fixed the Galactic absorption to the value reported in Dickey & Lockman (1990). The normalization of the model was left as a free parameter for both datasets. The plotted spectrum was derived with a grouping of 20 counts per bin. The best fit for a MEKAL model with untied normalizations is shown as a solid line. (Bottom panel) Fit residuals.

2.4 X-ray mass profile

In this work we recover the deprojected profiles of gas temperature and density without any parametrization of the ICM properties, which could introduce considerable systematic errors in the mass measurement results (Rasia et al. 2006). Our estimate relies on the assumptions of spherical symmetry and hydrostatic equilibrium and on the choice of an analytic model for the total mass. In the case of MS2137 these assumptions seem to be reasonable, since, e.g., the strongly peaked central surface brightness and a roughly circular X-ray emission can generally suggest a relaxed dynamical state.

Here we summarize the most relevant aspects of the technique we have applied; for full details, see Ettori, De Grandi & Molendi

(2002); Morandi, Ettori & Moscardini (2007); Morandi & Ettori (2007).

From the spectral analysis we derived for each annulus the projected gas temperature T_{ring} , metal abundance Z_{ring} and the normalization K of the model; the latter provides an estimate for the Emission Integral $EI = \int n_e n_p dV \simeq 0.82 \int n_e^2 dV$. To derive the value of these quantities in volume shells, one has to calculate the intersection of each volume shell with 2-dimensional annuli. Geometrical considerations (Kris, Cioffi & Canizares 1983; Buote 2000) allow to evaluate the intersections through an upper triangular matrix (V) where the last pivot represents the outermost annulus, under the assumption of spherical symmetry. In this way we can recover the deprojected values applying some array operations.

To calculate the deprojected density profile, we combined the spectral information and the cluster X-ray surface brightness (hereafter SB) profile. The SB provides an estimate of the volume-counts emissivity $F_{\text{bin}} \propto n_e^2 \text{T}(\text{bin})^{1/2} / D_L^2$. By comparing this observed profile to the values predicted by a thermal plasma model (with temperature and metallicity equal to the measured quantities and taking into account the effect of Galactic absorption) one can solve for the electron density. In this way, we obtain a gas density profile which is better resolved than a spectral-only profile (see the top panel of Fig. 3). We computed the SB in 35 circular annuli. They were derived from the X-ray flux image in the energy range [0.5–2.0] keV, thus similarly to the spectral extraction annuli (see § 2.3), but applying a binning of 1000 counts. The X-ray centroid is the same for both profiles. We rederived the mass estimate calculating the SB profile over the range [0.3 – 8.0] keV, to verify if the energy range choice would affect our results.

The total mass was then constrained as follows. The observed deprojected temperature profile in volume shells T_{shell} was obtained through the relations:

$$n_e = \left[(\mathbf{Vol}^T)^{-1} \# (EI/0.82) \right]^{1/2}, \quad (1)$$

$$\epsilon = (\mathbf{Vol}^T)^{-1} \# L_{\text{ring}}, \quad (2)$$

$$\epsilon T_{\text{shell}} = (\mathbf{Vol}^T)^{-1} \# (L_{\text{ring}} T_{\text{ring}}), \quad (3)$$

$$\epsilon Z_{\text{shell}} = (\mathbf{Vol}^T)^{-1} \# (L_{\text{ring}} Z_{\text{ring}}), \quad (4)$$

where the symbol $\#$ indicates a matrix product.

We compare it to the predicted temperature profile T_{pred} , obtained by inverting the equation of hydrostatic equilibrium between the dark matter potential and the potential of the intracluster plasma, i.e.:

$$-G\mu m_p \frac{n_e M_{\text{tot,model}}(< r)}{r^2} = \frac{d(n_e \times k T_{\text{pred}})}{dr}; \quad (5)$$

where n_e is the deprojected electron density. Our best-fit mass model was determined by comparing the observed T_{obs} profile to the predicted one, which depends on the mass model parameters. So we minimized:

$$\chi^2 = \sum_{\text{rings}} \left(\frac{T_{\text{obs}} - T_{\text{pred}}}{\sigma_{\text{obs}}} \right)^2. \quad (6)$$

The T_{pred} profile was rebinned to the spectral scale. In the bottom panel of Fig. 3 we show the projected temperature profile as determined by the spectral analysis, the deprojected best-fit profile and the deprojected, rebinned profile.

We assumed an NFW density profile, which can be expressed as:

$$\frac{\rho_{\text{NFW}}(r)}{\rho_c} = \frac{\delta_c}{(r/r_s)(1+r/r_s)^2}, \quad (7)$$

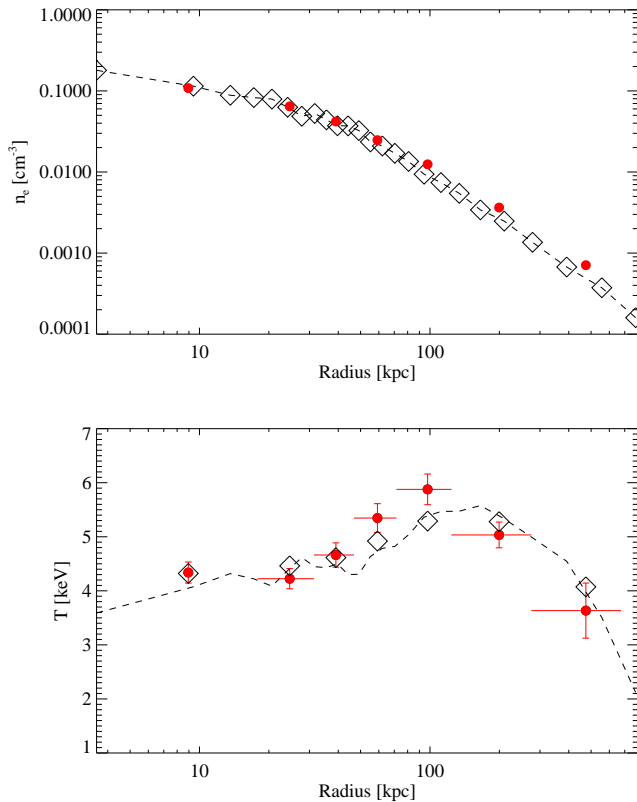


Figure 3. (Top panel) Deprojected gas density profile. Red circles mark the values determined by the normalization of the thermal spectra, diamonds represent the gas density values obtained combining both spectral and surface brightness measurements; the dashed line shows the best-fit profile. (Bottom panel) ICM temperature profile. Here we show the observed temperature profile (red circles, T_{obs} in the text), directly inferred from the spectral analysis, the deprojected temperature values (diamonds, T_{pred} in the text), rebinned to the same intervals of the observed profile, and the deprojected best-fit profile (dashed line). The small scale fluctuations of the temperature best-fit profile reflect the local variations in the gas density, since the condition of hydrostatic equilibrium is imposed between the smooth total mass profile and the gas pressure profile $P_{\text{gas}} \propto n_{\text{gas}} \times T_{\text{gas}}$ (see Eq. 5 in the text).

where r_s is the scale radius of the halo, δ_c is its characteristic overdensity and ρ_c is the critical density of the universe. We will define the NFW profile using the scale radius and the concentration parameter c_{200} , i.e. the ratio of the radius where the halo matter density is 200 times the critical density (r_{200}) to the scale radius: $c_{200} = r_{200}/r_s$.

The best-fit values are determined by minimizing the statistical estimator defined in Eq. 6. A first minimization is performed in the ranges $0.5 \leq c_{200} \leq 20.0$ and $10 \text{ kpc} \leq r_s \leq R_{\text{spat}}$ (where $R_{\text{spat}} \simeq 676 \text{ kpc}$ is the outer radius of the surface brightness profile). In this way a first estimate of the best-fit values is obtained. A second minimization is then performed in the $X_i \pm 3\sigma$ range, being X_i the mean values inferred through the first minimization. The mass model parameters obtained through our X-ray analysis, deriving the SB profile in the energy range $[0.5 - 2.0] \text{ keV}$, are:

BEST FIT X-RAY RESULTS				
r_s [kpc]	c_{200}	M_{200} [$10^{14} M_{\odot}$]	R_{200} [Mpc]	χ_{red}^2 [d.o.f.]
$162.72^{+18.6}_{-16.3}$	$8.68^{+0.7}_{-0.9}$	4.4 ± 0.3	1.41 ± 0.03	$2.1[5]$

The confidence levels for the NFW parameters are shown in Fig. 5. The choice of the energy range over which the surface brightness is estimated does not significantly affect our results: for example, deriving the SB profile in the wider range $[0.3 - 8.0] \text{ keV}$ we obtain the following values:

- (i) $r_s = 153.8^{+17.2}_{-20.7} \text{ kpc}$,
- (ii) $c = 8.93^{+1.0}_{-0.6}$,
- (iii) $M_{200} = 4.1 \pm 0.3 \times 10^{14} M_{\odot}$,
- (iv) χ_{red}^2 [d.o.f.] = $3.1[5]$.

The gas mass profile and the total mass profile are shown in Fig. 4. To indicate how much the X-ray mass profile depends on the choice of the density profile, in Fig. 4 we show also the mass profiles derived assuming two other parametric models, i.e. the Rasia-Tormen-Moscardini (hereafter RTM) profile (Rasia, Tormen & Moscardini 2004) and the King profile (King 1962). The RTM model was deduced from the direct analysis of non-radiative N -body hydro-simulations, without any assumption on the gas equation of state or on the cluster dynamical equilibrium. The resulting DM density distribution is:

$$\tilde{\rho}_R(r) = \frac{\rho_{0,R}}{r(r+r_*)^{1.5}}. \quad (8)$$

The King profile (King 1966; Rood et al. 1972) was derived under the assumption of an isothermal particle distribution, and can be expressed as:

$$\rho_K(r) = \frac{\rho_{0,K}}{(1 + (r/r_c)^2)^{3/2}}. \quad (9)$$

The mass estimates which were obtained adopting the RTM and the King mass model are $M_{200,\text{RTM}} = 5.1 \pm 0.3 \times 10^{14} M_{\odot}$ and $M_{200,\text{King}} = 2.2 \pm 0.2 \times 10^{14} M_{\odot}$. The corresponding χ_{red}^2 values are 3.7 and 4.1 (over 5 degrees of freedom), respectively. When assuming the RTM or the King density profile, the surface brightness was estimated in the energy range $[0.3 - 8.0] \text{ keV}$. The best-fitting model is the NFW profile, even though the RTM profile is not a significantly worse fit. Clearly, the extrapolated mass derived through a profile shallower in the external regions is lower than the mass estimates obtained with more cuspy parametrizations.

We have compared our X-ray estimate with the value predicted by the $M - T_X$ relation. For instance, Arnaud, Pointecouteau & Pratt (2005), through the analysis of 10 nearby, relaxed galaxy clusters observed with *XMM-Newton*, deduced the following relations for clusters with $kT \geq 3.5 \text{ keV}$:

$$h(z)M_{200} = 5.74 \times \frac{kT}{5 \text{ keV}}^{1.49},$$

$$h(z)M_{500} = 4.10 \times \frac{kT}{5 \text{ keV}}^{1.49},$$

where $h(z)$ is the Hubble constant normalised to its local value and kT is the spectroscopic temperature over the $[0.1 - 0.5] R_{200}$ region (corresponding to $[0.15 - 0.75] R_{500}$)⁵. The authors de-

⁵ Accurate predictions on the X-ray scaling relations are also presented in Nagai, Kravtsov & Vikhlinin (2007), through the results obtained by Vikhlinin et al. (2006) analysing *Chandra* observations of 13 low redshift,

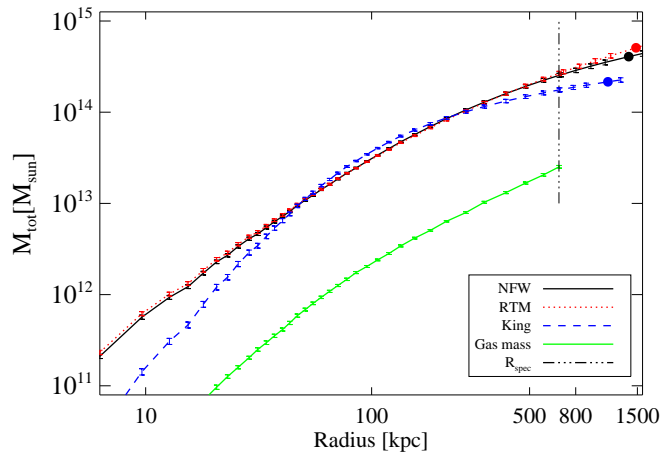


Figure 4. MS2137 total mass profiles, as determined through the X-ray analysis for different choices of parametrised mass models. The vertical line indicates the boundary of the spectral extraction, the filled circles mark the value of R_{200} for the corresponding mass profile. The measured gas mass profile is also shown as a green solid line.

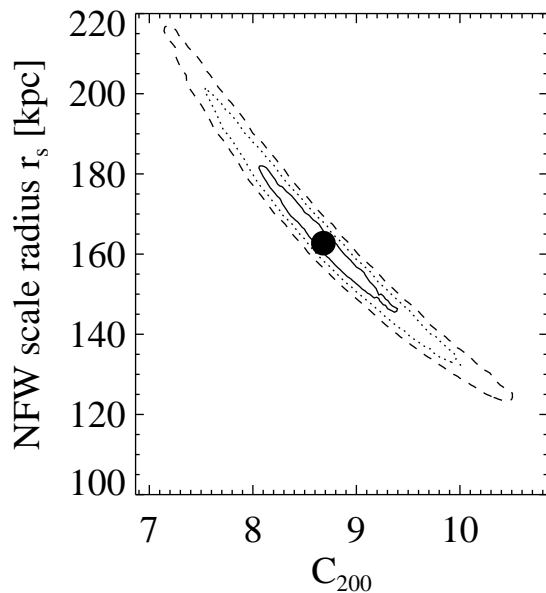


Figure 5. Confidence levels determined through the X-ray analysis for the NFW profile parameters c_{200} and r_s . The contours indicate the 1σ , 2σ and 3σ c.l., and the black circle marks the best-fit values.

derived the temperature T_X from a single-temperature fit to the integrated spectrum. The highest redshift cluster in the sample is

relaxed clusters. The scaling relations in Nagai et al. (2007) are calibrated with the gas temperature derived in the wider radial range $70 \text{ kpc} < r < R_{500}$. We applied the scaling relations found by Arnaud et al. (2005) to refer to a spatial range where our spectroscopic temperature estimate is more robust. However, Arnaud et al. (2005) asserted that their scaling relation estimates are very similar to those derived in Nagai et al. (2007), so our conclusions would be unchanged.

at $z \simeq 0.15$. We estimated the value of kT in a similar manner to Arnaud et al. (2005): we extracted the X-ray spectrum in the energy interval $[0.6 - 5] \text{ keV}$ and in the same radial range $[0.1 - 0.5]R_{200}$. We derived the value of $R_{200} = 1.37 \pm 0.04 \text{ Mpc}$ fitting the data with an NFW profile for a density contrast $\delta = 200$. We considered only the Obs. 928, due to the higher background in the external regions for Obs. 5250 (see § 2.3). The spectroscopic gas temperature over the spatial range $[0.1 - 0.5] R_{200}$ is $T_X = 4.1 \pm 0.3 \text{ keV}$ (the c -statistic value for the spectral fit is 293.2 over 296 degrees of freedom). This value leads to $M_{200, \text{scal}} \simeq 3.7 \times 10^{14} M_\odot$ and $M_{500, \text{scal}} \simeq 2.6 \times 10^{14} M_\odot$. These estimates are lower than ours (i.e. $M_{200} \simeq 4.4 \pm 0.3 \times 10^{14} M_\odot$ and $M_{500} \simeq 3.5 \pm 0.2 \times 10^{14} M_\odot$), but are compatible at a 4σ level with our results. The X-ray mass of MS2137 seems to be consistent with the $M-T_X$ scaling relation found for relaxed galaxy clusters.

3 STRONG LENSING ANALYSIS

3.1 Overview

MS2137.3–2353 is a well-known lensing system; the radial feature in its double-arc configuration is the first ever detected (Fort et al. 1992). The radial arc may be very useful in constraining the cluster central density slope. For axially symmetric lenses, the radial and tangential critical curves arise if $\lambda_r = 1 - (d/dx)(m/x)$ and $\lambda_t = 1 - m/x^2$ vanish, respectively, λ_r and λ_t being the eigenvalues of the Jacobian matrix of the lens mapping (see Bartelmann & Narayan 1995 for an extended review). Thus, the tangential and radial arc positions allow one to constrain the enclosed total mass and the mass distribution derivative, respectively. We carried out a strong lensing analysis on deep HST data retrieved from the Space Telescope Archive⁶. The data consists of a WFPC2 association image, taken with the F702W filter and obtained combining 10 exposures for a total integration time of 22.2 ks ⁷ (a portion of the HST image is shown in Fig. 6).

The tangential and radial arc distances from the BCG center are $\simeq 15$ and $\simeq 5 \text{ arcsec}$: the former is composed of two images with reverse parity (A01 and A02 in Fig. 6, following the notation of Gavazzi 2005b), associated with the counter-images A2 and A3. A fifth demagnified image lying near the center of the BCG is predicted if the central density slope is shallower than the isothermal model slope. Thus the position of the central image would provide an additional constraint on the inner density (for example, see the results of Gavazzi, Fort, Mellier, Pelló & Dantel-Fort 2003), and as a consequence on the BCG mass. However, the BCG-subtracted image presents residuals in the central region, where the fifth image, if present, is predicted. The noise level after the BCG subtraction makes a clear identification of the central image difficult. For these reasons the central counter-image was not included as an additional constraint.

Spectroscopic measurements (Sand, Treu & Ellis 2002) stated that the two groups of images arise from 2 different sources at redshift $z_{\text{tang}} = 1.501$ and $z_{\text{rad}} = 1.502$; recent data (Soucail, Covone & Kneib 2007) confirmed that the counter-image of the radial arc B1 is the feature B2 (see Fig. 6).

In the next section we will present a parametric strong lensing reconstruction of the cluster mass distribution, performed using the

⁶ archive.stsci.edu/

⁷ Proposal ID: 5402; PI: I.Gioia.

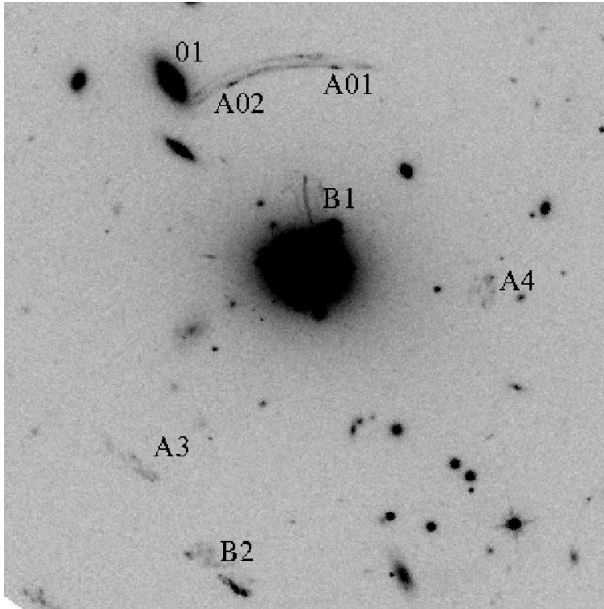


Figure 6. Multiple image interpretation of the lens system, overlotted on the HST/WFPC2 image of MS2137 (filter: F702W; number of combined images: 10; total integration time: 22.2 ks; proposal ID: 5402; PI: I.Gioia). The size of the field of view is $\simeq 42 \text{ arcsec} \times 45 \text{ arcsec}$; the coordinates of the images used as constraints in the strong lensing analysis are listed in Table 3.

Table 3. Coordinates of the multiple images considered in the MS2137 strong lensing modeling. Coordinates are in arcsec with respect to the BCG center. We did not include as constraint the fifth central image, that was not clearly identified. Spectroscopic measurements (Sand, Treu, Smith & Ellis 2004) indicate a redshift of $z_{\text{tang}} = 1.501$ and $z_{\text{rad}} = 1.502$ for the first and the second system, respectively.

MULTIPLE-IMAGE SYSTEMS								
Id	Im.1		Im.2		Im.3		Im.4	
1.a	-5.20	13.87	2.61	14.86	13.59	-1.08	-12.03	-15.29
1.b	-4.88	13.98	2.31	14.89	13.46	-1.26	-12.36	-14.94
1.c	-7.32	13.68	0.04	15.77	13.06	-2.96	-13.32	-13.63
1.d	-7.45	12.74	4.69	14.80	13.62	-2.13	-11.83	-15.00
1.e	-3.79	14.52	0.27	15.06	13.33	-1.40	-12.62	-14.71
1.f	-6.85	13.86	-1.35	15.71	12.93	-2.78	-13.51	-13.68
1.g	-7.81	13.26	1.32	15.82	12.86	-3.28	-13.32	-13.50
1.h	-5.70	14.55	-2.14	15.60	12.80	-3.06	-13.55	-13.53
1.i					13.13	-1.23	-13.28	-14.45
1.j					12.01	-2.12	-15.13	-12.80
1.k					-14.17	-13.40	12.50	-2.01
2.a	0.04	6.79	0.33	3.41	-7.28	-22.49		
2.b	0.00	6.44	0.27	3.88	-7.22	-22.75		
2.c	-0.06	5.87	0.17	4.21	-7.05	-22.88		
2.d	-0.03	5.28	0.10	4.50	-6.92	-23.04		

*Lenstool*⁸ analysis software (Kneib et al. 1996; Jullo et al. 2007).

3.2 Lens modeling

To identify the multiple image systems, we started by referring to the configuration provided by Gavazzi (2005b) (hereafter G05), the

most detailed knots catalogue available in the literature. We then iteratively refined the system by selecting several sets of ellipses, likely belonging to a common source area (their coordinates are listed in Table 3).

Our lens mass model consists of a cluster-scale mass component and of two galaxy-scale components, namely the BCG and the galaxy near the tangential arc. The latter (flagged 01 in Fig. 6) was included to account for its likely perturbative effect, due to its proximity to the tangential arc (Meneghetti et al. 2007). We modeled the cluster scale component using an elliptical NFW profile, as implemented in the *Lenstool* code (for a detailed discussion on the lens properties of this density profile, see Bartelmann 1996; Meneghetti, Bartelmann & Moscardini 2003b: for full details on the elliptical NFW implementation in *Lenstool* the reader can refer to Golse & Kneib 2002).

Our main clump model has seven free parameters: the coordinates of the center of mass (x_c, y_c), the ellipticity of the mass distribution (e), the position angle (θ), the characteristic velocity dispersion σ_0 and the NFW profile parameters (the concentration c_{200} and the scale radius r_s). The center of mass was initially set to the BCG centroid, but it was allowed to vary by ± 15 arcsec; the ellipticity and the position angle of the dark matter clump were also, as a first estimate, set equal to the BCG values, then were optimized in the ranges $[0.0 \leq e \leq 0.5]$ and $[130.0 \leq \theta \leq 160.0]$ degrees. The optimization ranges for the scale radius and the concentration parameter are $[50 \leq r_s \leq 650]$ kpc and $[0.5 \leq c_{200} \leq 20.0]$. The choice of these intervals is motivated by cluster analysis results from previous studies. Of course, strong lensing allows to constrain only the inner matter distribution, so the estimate of the virial radius - and therefore of the concentration parameter - using strong lensing alone is less robust; however, we decided not to fix any mass distribution parameter, but rather to sample them in wide ranges to avoid biasing our results.

The galaxies were modeled either as dual Pseudo Isothermal Elliptical Mass Distribution - hereafter dPIE - with a null core radius, or as elliptical singular isothermal sphere - hereafter SIE (see Natarajan & Kneib 1997, Limousin, Kneib & Natarajan 2005, Elíasdóttir et al. 2007 for the properties of these potentials and for full details on their implementation in the *Lenstool* code). Unlike the studies of Gavazzi (2005b); Sand et al. (2008), we did not model the BCG stellar velocity distribution in our analysis. We assumed a parametric model for the BCG mass (dPIE or SIE), so its mass is determined by the central velocity dispersion (and the scale/core radius values in the dPIE case). We are aware that stellar dynamics data would help to solve the existing degeneracy between the stellar mass and the mass of DM and gas in the cluster center. However, here we are more interested in determining the shape of the total mass profile at radii larger than those where the stellar mass is a non negligible mass component.

We fixed the galaxies ellipticity and orientation to the values derived by the HST image, using the IRAF external package *isophote* of the *stsdas* distribution. When modeling the galaxies as dPIE mass distribution, the values we imposed to the dPIE scale radius are almost the same of Sand, Treu, Ellis, Smith & Kneib (2008), so $r_{\text{cut,BCG}} = 22$ kpc and $r_{\text{cut,gal}} = 5$ kpc. The other free parameter in the galaxy optimization was the central velocity dispersion σ_0 ; the spectroscopic measurements obtained by Sand, Treu & Ellis (2002) with the Echelle Spectrograph and Imager on the Keck II telescope indicate a central value for the BCG stellar velocity of $\sigma_{\text{measured,BCG}} \simeq 325 \pm 35 \text{ km s}^{-1}$. However, the cD measured velocity dispersion cannot be directly related to the “characteristic” one in galaxy mass mod-

⁸ The code is available at the url www.oamp.fr/cosmology/lenstool.

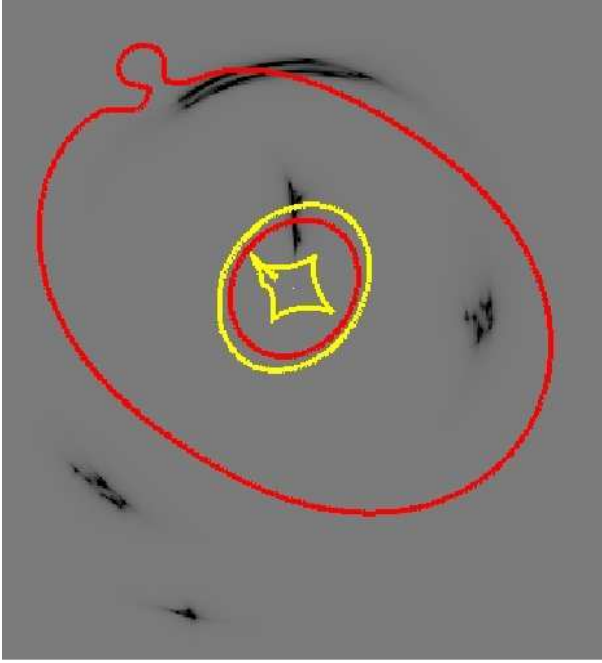


Figure 7. Images predicted by our best-fit lens model. In this case the galaxies included in the fit (i.e. the BCG and the galaxy flagged 01 in Fig. 6) were modeled as dPIE potentials. The size of the image is $\simeq 42 \text{ arcsec} \times 45 \text{ arcsec}$. The red [yellow] lines represent the critical [caustic] lines.

els, since the observed dispersion depends upon the unknown dark matter potential contribution to the stellar dynamics. The uncertainty on the velocity dispersion parameter could potentially introduce additional errors in the strong lensing modelling (Wu 1993). Despite of this, the BCG stellar mass is an important lens component (Meneghetti, Bartelmann & Moscardini 2003a, Hilbert et al. 2008), especially when modeling radial arcs, which, due to their position very close to the cluster center, are extremely sensitive to the cuspy distribution of luminous matter (see the earlier findings of Miralda-Escude 1995 on this topic). We thus imposed the measured $\sigma_{\text{measured,BCG}}$ as an upper limit for the velocity dispersion optimization range, and set as lower limit the value of $\sigma_{0,\text{BCG}} = 230 \text{ km s}^{-1}$, that is plausible given the high luminosity of the BCG. A discussion on the effect of this choice on the lensing results is presented in § 3.3.

The optimization procedure of the *Lenstool* code is performed in the source plane, by mapping the positions of the input multiple images back to the source plane, and requiring they have a minimal scatter (Jullo et al. 2007). The goodness-of-fit is evaluated through the following χ^2 estimator:

$$\chi^2 = \sum_j \chi_{\text{pos}}^2(j), \quad (10)$$

where the subscript j refers to the multiply imaged systems.

We assumed the uncertainty in the lensed image positions to be $\sigma_I = 0.3''$: mapping it back to the source plane one obtains an estimate of the error in the source plane.

3.3 Strong lensing results

The optimization and the error measurement are performed through the Bayesian optimization method implemented in *Lenstool*, im-

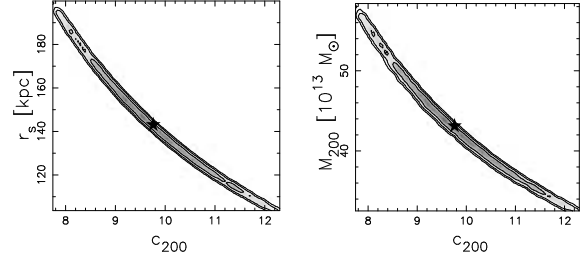


Figure 8. Confidence levels for the NFW mass model parameters determined through a strong lensing analysis. The contours show the parameter non-marginalized probability density, and refer to the model [1] in Table 4. [Left panel] NFW concentration parameter c_{200} vs the scale radius r_s ; [right panel] the concentration parameter vs the cluster total mass M_{200} , extrapolated up to R_{200} .

Table 5. Best fit parameters for the galaxies included in the lens system. The galaxies were parameterized as dPIE or SIE potentials in the lens model [1] and [2], respectively (in Tab. 4 we list the fit results for the other parameters of the lens model). We report the mode of the distributions, with the 68% statistical errors, and the best-fit values enclosed in round brackets. Values in square brackets were not optimized.

GALAXY MODEL PARAMETERS				
Model	Halo	Ellipticity	R_{cut} [kpc]	σ_0 [km s $^{-1}$]
[1]	BCG	[0.18]	[22.0]	$230.7^{+11.2}_{-0.49}$ (230.5)
	Galaxy	[0.38]	[5.0]	$150.2^{+26.5}_{-23.9}$ (159.2)
[2]	BCG	[0.18]	-	$231.4^{+33.3}_{-1.0}$ (240.3)
	Galaxy	[0.38]	-	$124.5^{+12.9}_{-16.5}$ (124.2)

posing an optimization rate of $\delta\lambda = 0.1$.

A summary of the best-fit values for two lens configurations is reported in Table 4.

In Table 5 we list the galaxy model values inferred through the strong lensing optimization. The configuration we will take as a reference in the following is labelled [1].

The lensed images predicted by the reference model are shown in Fig.7 and the corresponding likelihood contour levels for the NFW parameters are shown in Fig.8. In Table 6 are reported the χ^2 and the mean scatter for each image system.

The curvature of the radial arc, peculiar of this strong lensing system, is not well reproduced by our lens models. Due to its position very close to the cluster center, the radial arc is affected by the BCG mass and dynamics. Thus a possible explanation of the offset between the predicted and the observed radial arc curvature could be, e.g., the effect of a potential with non-constant ellipticity or position angle, that cannot be taken into account with the current mass model implementations (see Gavazzi et al. 2003). Other features of the arc (like its position or its radial extension) are quite well reproduced by our models. So, despite of the uncertainty on its curved shape, the radial arc provides indeed a tight constraint on the position of the radial critical line, and as a consequence on the total mass derivative in the cluster central region.

Resuming the strong lensing results, the best-fit models indicate a negligible shift of the cluster center with respect to the BCG centroid, and a slight offset between the BCG and the cluster halo projected orientation, $\Delta\theta \simeq 5^\circ$, which is lower than the $\Delta\theta \simeq 13^\circ$ found by G05 and by Sand et al. (2008). Such a misalignment could have either a geometrical explanation (e.g. the projection effect

Table 4. Best fit parameters, obtained for different lens models. Hereafter, we will refer to the first model as the reference model. Quoted errors correspond to 1σ confidence level. The columns indicate the lens configuration (the cluster halo model + the galaxy model), the coordinates of the center of mass, expressed in arcsec with respect to the BCG centroid, the ellipticity and position angle (WCS aligned) of the cluster clump, the scale radius and the concentration parameter (both referred to a halo overdensity of 200), the extrapolated mass up to R_{200} , the characteristic velocity dispersion of the NFW profile implementation in *Lenstool* and the total χ^2 , calculated over 15 knots systems, for a total of 50 image areas. When the best-fit value is significantly different from the mode of the distribution, the former is reported enclosed in brackets. The errors on x_c, y_c and on the ellipticity are $\simeq 0.1$ and $\simeq 0.01$, respectively. Ellipticity e here is expressed as $(a^2 - b^2)/(a^2 + b^2)$.

BEST FIT STRONG LENSING RESULTS									
Model	x_c [arcsec]	y_c [arcsec]	e	θ [deg]	r_s [kpc]	c_{200}	M_{200} [$10^{14} M_\odot$]	σ_0 [km s^{-1}]	χ^2_{tot} [d.o.f.]
[1] NFW+dPIE	0.0	0.0	0.10	$147.2^{+0.6}_{-0.4}$ [147.4]	$148.9^{+22.0}_{-24.7}$ [143.5]	$9.50^{+1.29}_{-0.87}$ [9.76]	$4.11^{+0.75}_{-0.46}$ [4.31]	$1377.3^{+26.9}_{-36.2}$ [1366.4]	17.6[61]
[2] NFW+SIE	0.1	-0.1	0.10	149.3 ± 0.7 [149.2]	$118.3^{+26.0}_{-14.3}$ [117.3]	$10.47^{+1.26}_{-1.23}$ [10.98]	$3.38^{+0.59}_{-0.35}$ [3.36]	$1291.2^{+28.9}_{-20.5}$	10.9[61]

Table 6. The results of the source plane optimization performed with the *Lenstool* code for our reference model, labelled [1] in Table 4. The columns list the knots system, the χ^2 of the system, the root-mean-square computed in the source plane (rms_s) and the corresponding one in the image plane (rms_i). The last row reports the total χ^2 estimator, referring to a model with 61 degrees of freedom.

GOODNESS OF FIT			
System	χ^2	rms_s ["]	rms_i ["]
1.a	0.48	0.034	0.27
1.b	1.72	0.064	0.37
1.c	2.18	0.075	0.22
1.d	0.90	0.053	0.23
1.e	1.80	0.062	0.50
1.f	1.61	0.062	0.86
1.g	1.06	0.057	0.37
1.h	0.21	0.021	0.25
1.i	0.11	0.030	0.08
1.l	0.16	0.038	0.10
1.m	0.14	0.034	0.07
2.a	3.40	0.168	0.33
2.b	1.97	0.114	0.35
2.c	1.13	0.078	0.28
2.d	0.75	0.057	0.44
Total	χ^2 [d.o.f.] 17.62 [61]	rms_s ["] 0.072	rms_i ["] 0.39

of a prolate halo -see G05- or the difference of halos triaxialities (Keeton, Kochanek & Seljak 1997)) or a dynamical origin, linked to the BCG formation process (Quadri, Möller & Natarajan 2003; see also Minor & Kaplinghat 2007).

To estimate the magnitude of the systematic error on the lensing mass introduced by the uncertainty on the velocity dispersion, we optimized again the lens model imposing as lower limit $\sigma_{0,\text{BCG}} =$

325 km/s. Under these conditions we derived the following values:

Parameter	Unit	Mode	Best fit
x_c	arcsec	0.2 ± 0.1	
y_c	arcsec	0.2 ± 0.1	
e		0.11 ± 0.01	
θ	deg	$146.2^{+0.4}_{-0.4}$	
r_s	kpc	$153.1^{+23.3}_{-19.5}$	[160.1]
c_{200}		$9.21^{+0.92}_{-0.86}$	[8.93]
M_{200}	$10^{14} M_\odot$	$4.40^{+0.6}_{-0.5}$	[4.59]
$\sigma_{0,\text{halo}}$	km s^{-1}	$1359.0^{+31.3}_{-25.5}$	
$\sigma_{0,\text{BCG}}$	km s^{-1}	$327.0^{+3.2}_{-0.15}$	[325.4]
χ^2_{tot} [d.o.f.]		61.1 [61]	

The values in square brackets indicate the best-fit results if they are significantly different from the mode of the distribution. The parameter values in this case are within 2σ respect to the ones presented in Tab. 4. The results obtained decreasing the BCG velocity dispersion (and thus its mass) are shown in § 5. So, considering the results obtained for the two boundary conditions (no halo contribution to the BCG potential well and no mass in the BCG) we can estimate that, regard to the strong lensing mass, the systematic errors associated with the uncertainty in the BCG mass account for an additional $\simeq 25\%$ in the final error budget. We would like to stress again that this additional error component arises in the case of galaxy clusters with central lensed features, when trying to disentangle the central galaxy mass from the underlying halo mass and when *no additional constraint* (e.g. the BCG stellar dynamics) is included.

Anyway the NFW parameters are quite well constrained by the cluster strong lensing features, and we did not detect a high concentration for this cluster, as stated in previous works in the literature (see Comerford & Natarajan 2007 and § 5 for further discussion).

4 X-RAY AND STRONG LENSING COMPARISON

Coupling the X-ray and lensing mass estimates is not a trivial task, as already stated by G05, due to their different dependencies on the characteristics of galaxy clusters (like asphericity) as well as for the still incomplete treatment of the biases that could affect both measurements. Though joint analyses of homogeneous effects (e.g. weak and strong lensing) often supply converging estimates, lead-

Table 7. Best fit parameters for the NFW profile. The strong lensing results refer to the reference model, labeled [1] in Tab. 4. Quoted errors correspond to 1σ confidence level. For a comparison, we reported the results obtained in some earlier representative studies: the original values were converted according to common definitions. We list here the findings obtained by Allen et al. (2001) and Schmidt & Allen (2007) through the X-ray analysis of *Chandra* data (columns A01 and S07, respectively) and by Gavazzi (2005b) and Comerford et al. (2006) through a strong lensing study (columns G05 and C06, respectively). Here, again, $e = (a^2 - b^2)/(a^2 + b^2)$.

COMPARISON WITH PREVIOUS RESULTS							
	X-RAY	SL	A01	S07	G05	C06	Units
r_s	$162.72^{+18.60}_{-16.27}$	$148.9^{+22.0}_{-24.7}$	160.0 ± 30	180.0 ± 20.0	158.0^{+15}_{-13}	91.4 ± 3	kpc
c_{200}	$8.68^{+0.71}_{-0.91}$	$9.50^{+1.29}_{-0.87}$	$8.71^{+1.22}_{-0.92}$	$8.19^{+0.54}_{-0.56}$	$11.92^{+0.77}_{-0.74}$	13.0 ± 1.0	-
M_{200}	4.43 ± 0.25	$4.11^{+0.75}_{-0.46}$	-	-	$7.56^{+0.63}_{-0.54}$	2.9 ± 0.4	$10^{14} M_\odot$
e	-	0.1 ± 0.01	-	-	0.25	0.12	-

ing to remarkable results (Bradač et al. 2005, 2006; Limousin et al. 2007; Merten et al. 2008), comparing 2- and 3-dimensional measurements requires further caution. Recently, several interesting attempts have been made to infer cluster masses through multi-wavelength, combined analysis (Mahdavi et al. 2007), in some cases suggesting that a direct comparison needs further investigation (Lemze et al. 2008). We decided instead to perform two parallel analyses to understand if these methods lead to discrepant mass estimates for MS2137.

We found that our X-ray and strong lensing results are in good agreement: both the extrapolated value of the total mass M_{200} and the mass model parameters agree within the 2σ range. The parameter probability distributions are mutually consistent (see the left panel of Figure 9), although the concentration inferred from the lensing analysis is slightly higher than the X-ray one. A mild elongation of the cluster along the line of sight could be a possible explanation, as already suggested by G05. Another reason could be the additional uncertainty associated to the BCG mass. To evaluate the differences between the X-ray and the strong lensing results, we show in the right panel of Figure 9 the projected total mass enclosed in concentric cylinders inferred from both analyses. The assessment of the errors on the strong lensing mass was performed by stacking 500 mass map realizations, obtained through the *Lenstool* Bayesian optimization, and computing the standard deviation at each map point.

5 COMPARISON WITH PREVIOUS STUDIES

In this section we will briefly compare our results with some previous studies, namely the findings obtained by Schmidt & Allen (2007) (hereafter S07) and Allen, Schmidt & Fabian (2001) (hereafter A01) through the X-ray analysis of *Chandra* data, and those inferred through a strong lensing analysis by G05 and Comerford et al. (2006) (hereafter C06; see also Gavazzi et al. 2003; Comerford & Natarajan 2007; Shu et al. 2008).

S07 studied the same two *Chandra* datasets considered in this work, whereas the analysis of A01 was carried out on the only *Chandra* dataset available at that epoch (Obs. 928). The method applied in their studies are similar to ours. Briefly, S07 and A01 derived the observed X-ray surface brightness profile and the de-projected X-ray gas temperature profile, and combined them to determine the gas mass and total mass profile of the galaxy cluster, under the assumptions of hydrostatic equilibrium and spheri-

cal symmetry⁹ (for more details, see also White, Jones & Forman 1997; Allen, Ettori & Fabian 2001). The gas temperature and density profiles for the single case of MS2137 were not listed in S07 and A01, since in both cases the authors presented the results of careful analyses of large samples of objects. Thus a direct comparison of the derived profiles was not possible. Concerning the final estimates of the NFW parameters, there is a good matching between our results and the values presented both in S07 and A01. Despite some differences in the analyses (for example the spectral binning and the X-ray background estimate) the results are mutually consistent within a 2σ level (see Tab.7).

A comparison with the previous strong lensing analyses involves an extended discussion, since, as already stated by Comerford & Natarajan (2007), the scatter in the differing results found in the literature regarding this cluster is quite large. A complete discussion on this topic is beyond the aim of this paper: here we will simply compare the results and the methods of analysis, and possibly suggest some explanations. For full details on the basis of the optimization methods, the reader can refer to the related papers, Gavazzi (2005b) and Comerford et al. (2006) respectively. Both the analyses of G05 and C06 were performed exploiting their own inversion codes. The source plane χ^2 estimator adopted in G05 follows the χ_s^2 definition in the *lensmodel* software (Keeton 2001a,b). G05 reported a value for the scale radius r_s consistent with our estimate, whereas there is disagreement between our estimates of the halo concentration and mass. We couldn't find a convincing explanation for the difference in our results.

The code utilised in C06 optimizes the lens model parameters by minimizing a figure-of-merit function, defined as the sum of three components both in the image and in the source planes. The optimization procedure is meant to shrink: (i) the distance between each data point position and the nearest predicted one, (ii) the distance between the predicted point positions and the nearest data point (thus penalising models that produce unobserved images) and (iii) the size and noncompactness of the predicted sources (see C06 and Shu et al. 2008 for a detailed discussion).

This fitting technique is very accurate: however, in their analysis C06 modeled the lens as a single elliptical NFW potential, not including any galaxy component. Thus, the free parameters of their lens model are the scale radius r_s , the ellipticity, the position angle θ and the scale convergence $k_s \equiv \rho_s r_s / \Sigma_{\text{crit}}$, where

⁹ S07 carried out two separate mass analyses, deriving a mass estimate of the cluster total matter and of its three components (dark matter, gas and cD galaxy). In the following, we will refer to the results obtained in the first case.

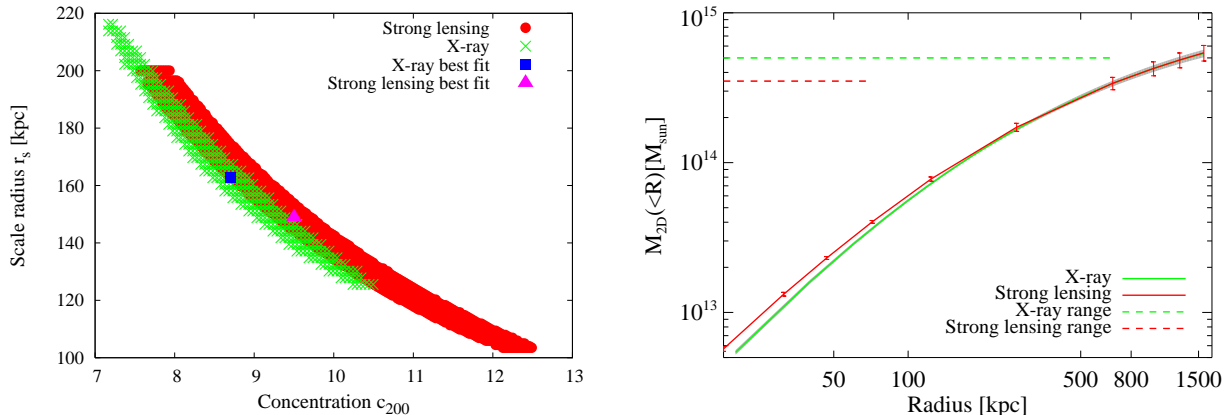


Figure 9. [Left panel] 3σ marginalized probability distribution for the NFW parameters - concentration and scale radius. The regions refer to the the X-ray (drawn in green) and strong lensing (drawn in red) results. The square [triangle] indicates the X-ray [strong lensing] best fit values. [Right panel] Projected total mass enclosed in cylinders of radius R . The solid green line represents the projected total mass profile derived through the X-ray analysis (the grey area indicates the 1σ region), the red line with error bars show the result of the strong lensing analysis. The error bars indicate the 1σ errors inferred from the Bayesian optimization. The green [red] dashed horizontal line indicates the spatial range over which the X-ray [strong lensing] analysis has been performed.

as usual Σ_{crit} represents the critical surface mass density. The resulting MS2137 mass parameters are $r_s \simeq 91.4 \pm 3$ kpc and $c \simeq 13.0 \pm 1.0$, leading to a total mass extrapolated up to R_{200} of $M_{200} \simeq 2.9 \pm 0.4 \times 10^{14} M_{\odot}$. Thus, the total mass and scale radius estimates of C06 are lower and their inferred concentration parameter is higher than our best-fit values.

We performed a single mass component analysis, in analogy with C06 and Shu et al. (2008). The best-fit values we obtained in this case are:

- (i) $r_s = 92.8 \pm 10.0$ kpc,
- (ii) $c = 13.5 \pm 1.1$,
- (iii) $M_{200} = 3.1 \pm 0.3 \times 10^{14} M_{\odot}$,

which are in excellent agreement with the C06 values; the total χ^2 is 29.6 for 63 d.o.f. This result highlights once again that the BCG has a non-negligible effect on strong lensing properties (Hilbert et al. 2008) when dealing with lensed features sensitive to the central mass distribution, such as radial arcs. Ignoring the BCG stellar mass component can return an ‘‘artificial’’ high-concentrated profile, to account for the missing central galactic component.

6 DISCUSSIONS AND CONCLUSIONS

We have presented new X-ray and strong lensing mass measurements for the galaxy cluster MS2137.3-2353, taking advantages of the high-resolution *Chandra* and *HST* data. Our X-ray analysis benefits from a non-parametric study of the gas temperature and density profiles. By combining them, we have recovered the cluster mass profile adopting the NFW model, under the assumptions of spherical symmetry and hydrostatic equilibrium.

The strong lensing reconstruction was performed through the publicly available code *Lenstool* (Kneib et al. 1996; Jullo et al. 2007), which allowed for a parametric analysis comparable to our X-ray study. Our mass estimates are consistent within the errors, leading to a mean value of the total mass, extrapolated up to R_{200} , of $\simeq 4.4 \pm 0.3 \times 10^{14} M_{\odot}$. We did not find a strong discrepancy between the strong lensing and the X-ray NFW parameter results, since the best-fit values mutually agree at a 3σ confidence level. The probability distributions are mutually compatible. The slight

difference in the allowed parameter space could be explained, for example, by a mild cluster elongation along the line of sight, which would affect mainly the strong lensing results. Moreover, the uncertainty on the BCG mass determination could introduce a systematic bias in the lensing measurements that we could quantify as an additional uncertainty of $\simeq 25\%$, since the extrapolated strong lensing mass estimate in this case depends upon the BCG stellar mass budget.

The agreement between these two mass estimates for a relaxed cluster, like MS2137, supports the statement that, for this kind of system, both the strong lensing and the X-ray analyses provide an unbiased way to estimate the cluster mass. As a general observation on the physics of this cluster, the convergence of these mass results implies that its main pressure support mechanism against gravity is the thermal pressure, so the assumption of hydrostatic equilibrium is verified. Non-thermal processes, such as turbulent motions or magnetic field effects, seemingly have little impact on the equilibrium state for this cluster, that appears a good example of relaxed cluster prototype. To verify if MS2137 represents a peculiar case in the cluster mass discrepancy debate, or if the relaxed dynamical state constitutes a sufficient condition for the convergence of the strong lensing and X-ray mass estimates, further investigations of both single cluster cases and large uniform samples are fundamental, and would provide new, useful insights on the galaxy cluster physics.

7 ACKNOWLEDGMENTS

We would like to thank Raphaël Gavazzi, Bernard Fort, Mario Radovich, Fabio Gastaldello, Giovanni Covone, Eric Jullo and Marceau Limousin for their help and suggestions. We are grateful to Matthias Bartelmann for reading the paper and providing useful comments. We thank the anonymous referee for useful comments and remarks that improved the presentation of our work. AD acknowledges the support of European Association for Research in Astronomy (MEST-CT-2004-504604 Marie Curie - EARA EST fellowship), and thanks Raphaël Gavazzi and Bernard Fort for their kind hospitality during the visit at IAP - Institut d’Astrophysique de Paris. AD also thanks Daniela Crociani and Ashley J. Ruiter

for their help and support. We thank Jean Paul Kneib and the *Lenstool* developers for making their lensing software public. This research has made use of data obtained from the *Chandra* Data Archive and of the software provided by the *Chandra* X-ray Center (CXC), and of *HST* data obtained from the MAST archive. We acknowledge the financial contribution from contracts ASI-INAF I/023/05/0, I/088/06/0 and I/016/07/0.

REFERENCES

- Allen S. W., 1998, *MNRAS*, 296, 392
- Allen S. W., Etori S., Fabian A. C., 2001, *MNRAS*, 324, 877
- Allen S. W., Schmidt R. W., Fabian A. C., 2001, *MNRAS*, 328, L37
- Arnaud K. A., 1996, in Jacoby G. H., Barnes J., eds, *Astronomical Data Analysis Software and Systems V* Vol. 101 of *Astronomical Society of the Pacific Conference Series*, XSPEC: The First Ten Years. pp 17–+
- Arnaud M., Pointecouteau E., Pratt G. W., 2005, *A&A*, 441, 893
- Bartelmann M., 1996, *A&A*, 313, 697
- Bartelmann M., Narayan R., 1995, in Holt S. S., Bennett C. L., eds, *Dark Matter* Vol. 336 of *American Institute of Physics Conference Series*, *Gravitational Lensing and the Mass Distribution of Clusters*. pp 307–+
- Borgani S., 2006, *ArXiv e-prints*, astro-ph/0605575
- Bradač M., Clowe D., Gonzalez A. H., Marshall P., Forman W., Jones C., Markevitch M., Randall S., Schrabback T., Zaritsky D., 2006, *ApJ*, 652, 937
- Bradač M., Erben T., Schneider P., Hildebrandt H., Lombardi M., Schirmer M., Miralles J.-M., Clowe D., Schindler S., 2005, *A&A*, 437, 49
- Bradač M., Schrabback T., Erben T., McCourt M., Million E., Mantz A., Allen S., Blandford R., Halkola A., Hildebrandt H., Lombardi M., Marshall P., Schneider P., Treu T., Kneib J.-P., 2008, *ApJ*, 681, 187
- Buote D. A., 2000, *ApJ*, 539, 172
- Comerford J. M., Meneghetti M., Bartelmann M., Schirmer M., 2006, *ApJ*, 642, 39
- Comerford J. M., Natarajan P., 2007, *MNRAS*, 379, 190
- Dalal N., Keeton C. R., 2003, *ArXiv e-prints*, astro-ph/0312072
- Diaferio A., Schindler S., Dolag K., 2008, *Space Science Reviews*, 134, 7
- Dickey J. M., Lockman F. J., 1990, *ARA&A*, 28, 215
- Elíasdóttir Á., Limousin M., Richard J., Hjorth J., Kneib J.-P., Natarajan P., Pedersen K., Jullo E., Paraficz D., 2007, *ArXiv e-prints*, astro-ph/07105636, 710
- Etori S., De Grandi S., Molendi S., 2002, *A&A*, 391, 841
- Etori S., Lombardi M., 2003, *A&A*, 398, L5
- Fort B., Le Fevre O., Hammer F., Cailloux M., 1992, *ApJ*, 399, L125
- Gao L., Navarro J. F., Cole S., Frenk C. S., White S. D. M., Springel V., Jenkins A., Neto A. F., 2008, *MNRAS*, 387, 536
- Gavazzi R., 2005a, in Mellier Y., Meylan G., eds, *Gravitational Lensing Impact on Cosmology* Vol. 225 of *IAU Symposium*, *Lensing & Dynamics in the Galaxy Cluster MS2137-23*. pp 179–184
- Gavazzi R., 2005b, *A&A*, 443, 793
- Gavazzi R., Fort B., Mellier Y., Pelló R., Dantel-Fort M., 2003, *A&A*, 403, 11
- Gitti M., Piffaretti R., Schindler S., 2007, *A&A*, 472, 383
- Golse G., Kneib J.-P., 2002, *A&A*, 390, 821
- Halkola A., Hildebrandt H., Schrabback T., Lombardi M., Bradač M., Erben T., Schneider P., Wuttke D., 2008, *A&A*, 481, 65
- Hallman E. J., Motl P. M., Burns J. O., Norman M. L., 2006, *ApJ*, 648, 852
- Hilbert S., White S. D. M., Hartlap J., Schneider P., 2008, *MNRAS*, pp 471–+
- Jing Y. P., Suto Y., 2000, *ApJ*, 529, L69
- Jullo E., Kneib J.-P., Limousin M., Elíasdóttir Á., Marshall P. J., Verdugo T., 2007, *New Journal of Physics*, 9, 447
- Kaastra J. S., Mewe R., 1993, *A&A Supp.*, 97, 443
- Keeton C. R., 2001a, *ArXiv e-prints*, astro-ph/0102341
- Keeton C. R., 2001b, *ArXiv e-prints*, astro-ph/0102340
- Keeton C. R., Kochanek C. S., Seljak U., 1997, *ApJ*, 482, 604
- King I., 1962, *AJ*, 67, 274
- King I. R., 1966, *AJ*, 71, 64
- Kneib J.-P., Ellis R. S., Smail I., Couch W. J., Sharples R. M., 1996, *ApJ*, 471, 643
- Kriss G. A., Cioffi D. F., Canizares C. R., 1983, *ApJ*, 272, 439
- Lemze D., Barkana R., Broadhurst T. J., Rephaeli Y., 2008, *MNRAS*, 386, 1092
- Limousin M., Kneib J.-P., Natarajan P., 2005, *MNRAS*, 356, 309
- Limousin M., Richard J., Jullo E., Kneib J.-P., Fort B., Soucail G., Elíasdóttir Á., Natarajan P., Ellis R. S., Smail I., Czoske O., Smith G. P., Hudelot P., Bardeau S., Ebeling H., Egami E., Knudsen K. K., 2007, *ApJ*, 668, 643
- Mahdavi A., Hoekstra H., Babul A., Sievers J., Myers S. T., Henry J. P., 2007, *ApJ*, 664, 162
- Markevitch M., Bautz M. W., Biller B., Butt Y., Edgar R., Gaetz T., Garmire G., Grant C. E., Green P., Juda M., Plucinsky P. P., Schwartz D., Smith R., Vikhlinin A., Virani S., Wargelin B. J., Wolk S., 2003, *ApJ*, 583, 70
- Meneghetti M., Argazzi R., Pace F., Moscardini L., Dolag K., Bartelmann M., Li G., Oguri M., 2007, *A&A*, 461, 25
- Meneghetti M., Bartelmann M., Moscardini L., 2003a, *MNRAS*, 346, 67
- Meneghetti M., Bartelmann M., Moscardini L., 2003b, *MNRAS*, 340, 105
- Merten J., Cacciato M., Meneghetti M., Mignone C., Bartelmann M., 2008, *ArXiv e-prints*, astro-ph/0806196, 806
- Mewe R., Gronenschild E. H. B. M., van den Oord G. H. J., 1985, *A&A Supp.*, 62, 197
- Minor Q. E., Kaplinghat M., 2007, *ArXiv e-prints*, astro-ph/07112537, 711
- Miralda-Escude J., 1995, *ApJ*, 438, 514
- Moore B., Governato F., Quinn T., Stadel J., Lake G., 1998, *ApJ*, 499, L5+
- Morandi A., Etori S., 2007, *MNRAS*, pp 708–+
- Morandi A., Etori S., Moscardini L., 2007, *MNRAS*, 379, 518
- Nagai D., Kravtsov A. V., Vikhlinin A., 2007, *ApJ*, 668, 1
- Natarajan P., Kneib J.-P., 1997, *MNRAS*, 287, 833
- Navarro J. F., Frenk C. S., White S. D. M., 1995, *MNRAS*, 275, 720
- Navarro J. F., Frenk C. S., White S. D. M., 1997, *ApJ*, 490, 493
- Ota N., Pointecouteau E., Hattori M., Mitsuda K., 2004, *ApJ*, 601, 120
- Quadri R., Möller O., Natarajan P., 2003, *ApJ*, 597, 659
- Rasia E., Etori S., Moscardini L., Mazzotta P., Borgani S., Dolag K., Tormen G., Cheng L. M., Diaferio A., 2006, *MNRAS*, 369, 2013
- Rasia E., Tormen G., Moscardini L., 2004, *MNRAS*, 351, 237
- Rood H. J., Page T. L., Kintner E. C., King I. R., 1972, *ApJ*, 175, 627

- Sand D. J., Treu T., Ellis R. S., 2002, *ApJ*, 574, L129
- Sand D. J., Treu T., Ellis R. S., Smith G. P., Kneib J.-P., 2008, *ApJ*, 674, 711
- Sand D. J., Treu T., Smith G. P., Ellis R. S., 2004, *ApJ*, 604, 88
- Schmidt R. W., Allen S. W., 2007, *MNRAS*, 379, 209
- Shu C., Zhou B., Bartelmann M., Comerford J. M., Huang J. ., Mellier Y., 2008, *ArXiv e-prints*, astro-ph/08051148, 805
- Smail I., Ellis R. S., Dressler A., Couch W. J., Oemler A. J., Sharples R. M., Butcher H., 1997, *ApJ*, 479, 70
- Soucail G., Covone G., Kneib J.-P., 2007, in Kissler-Patig M., Walsh J. R., Roth M. M., eds, *Science Perspectives for 3D Spectroscopy A VIMOS-IFU Survey of $z \sim 0.2$ Massive Lensing Galaxy Clusters: Constraining Cosmography*. pp 181+
- Stoche J. T., Morris S. L., Gioia I. M., Maccacaro T., Schild R., Wolter A., Fleming T. A., Henry J. P., 1991, *ApJS*, 76, 813
- Tozzi P., 2007, in Papantonopoulos L., ed., *The Invisible Universe: Dark Matter and Dark Energy Vol. 720 of Lecture Notes in Physics*, Berlin Springer Verlag, *Cosmological Parameters from Galaxy Clusters: An Introduction*. pp 125+
- Vikhlinin A., Kravtsov A., Forman W., Jones C., Markevitch M., Murray S. S., Van Speybroeck L., 2006, *ApJ*, 640, 691
- Voigt L. M., Fabian A. C., 2006, *MNRAS*, 368, 518
- Voit G. M., 2005, *Reviews of Modern Physics*, 77, 207
- White D. A., Jones C., Forman W., 1997, *MNRAS*, 292, 419
- Wilms J., Allen A., McCray R., 2000, *ApJ*, 542, 914
- Wu X.-P., 1993, *ApJ*, 411, 513
- Wu X.-P., Fang L.-Z., 1996, *ApJ*, 467, L45+